Electronic Supplementary Information (ESI)

Efficient design and synthesis of an amorphous conjugated polymer network for a metal-free electrocatalyst of hydrogen evolution reaction

Wakana Hamada,[a] Mafumi Hishida,[b] Ryuto Sugiura,[a] Haruka Tobita,[a] Hiroaki Imai,[a] Yasuhiko Igarashi,[c] and Yuya Oaki*,[a]

[a] Department of Applied Chemistry, Faculty of Science and Technology, Keio University, 3-14-1 Hiyoshi, Kohoku-ku, Yokohama 223-8522, Japan.

[b] Department of Chemistry, Faculty of Science, Tokyo University of Science, 1-3 Kagurazaka, Shinjuku, Tokyo 162–8601, Japan

[c] Faculty of Engineering, Information and Systems, University of Tsukuba, 1-1-1 Tennodai, Tsukuba 305-8573, Japan.

Email: oakiyuya@applc.keio.ac.jp

Contents

Experimental methods

Construction of the ΔE prediction model. The training dataset was prepared based on the literature data (Scheme S1 and Table S2).[11,38,49,55–63] The repeating units with the low molecular weight were extracted from the macromolecules. ΔE at -10 mA cm^{-2} as the objective variables (y) were extracted from the LSV curves in the literatures. The explanatory variables x_n (n = 1–7, 9, 10) in Table 1 were calculated by density function theory (DFT) using Gaussian 16 under B3LYP functional and 6–31G (d,p) basis set. The HSP distance x_8 was calculated by a commercial software HSP-iP. ES-LiR was performed on the training dataset to obtain the weight diagram.[22] The detailed method and algorithm were referred to our previous work.[24] The regression model was constructed using the extracted and selected x_n. The estimated ΔE was calculated using eqn (1).

Polymerization of BQ and furane derivatives. Mixture of *p*-benzoquinone (BQ, TCI, 98.0 %) and furane derivatives was prepared in a glass vial and then heated under microwave irradiation (Anton Parr, Monowave 400) for 1 h. BQ (1.5 g) and Fu (TCI 99.0 %, 1 cm^3) was heated at 120 °C. BQ (1.0 g) and BF (TCI 99.0 %, 1 cm^3) was heated at 200 °C. BQ (1.7 g) and Ox (TCI 98.0 %, 1 cm^3) was heated at 170 °C. BQ (1.0 g) and BO (TCI 99.0 %, 1.1 g) was heated at 200 °C. Solvent was not added in these precursors. The resultant precipitates were rinsed with acetone and then vacuum-dried at 190 °C for 6 h to remove the remaining monomers and oligomers. The resultant precipitate was used as the product.

The BQ-BO polymer was dispersed in ethylbenzene (15 mg BQ-BO in 20 cm^3) (Wako 96.0 %) or acetone (7 mg BQ-BO in 10 cm^3) (Kanto 99.5 %). The probe of an ultrasonic homogenizer was put in the dispersion liquid and then dispersion treatment was performed for 30 min for acetone and 1 h for ethylbenzene.

Structural characterization. An increase in the molecular weight was studied using TG under air atmosphere (Shimadzu DTA-60) with 10 K min^{-1}. The molecular structures of the resultant polymers and reference samples were analyzed by FT-IR (Jasco FT-IR 4200) with KBr method, XPS (Thermo Fisher Nexa), ^{13}C NMR (Bruker Advance Neo-400) with CP/MAS method. The extension of the conjugated length was studied by UV-Vis-NIR (Jasco V-650) and Raman (Renishaw In Via Raman) with excitation at 632 nm. The crystallinity was characterized by XRD (Bruker D8 Advance). The powder was filled in a crystalline silicon sample holder without diffraction peaks in the measuring range. The morphology of BQ-BO was observed using SEM (JEOL JSM-7100-F) operated at 5.0 kV and TEM (FEI Tecnai G2) operated at 200 kV. The particle-size distribution was measured using the dispersion liquid by DLS (Ohtsuka Electronics ELSZ-2000). The following reference samples were used for the structural and electrochemical characterization: GO (Aldrich), GC (Aldrich), r-GO (Stream Chemicals), and PPy (Aldrich). BQ-Py polymer was synthesized by the method in our previous report.[11]

Electrochemical properties. The dispersion liquid of BQ-BO powder (15 mm^3) was dropped on a GC electrode (3 mm in diameter). No other additives were used. After drying, the working electrode was set in a twin-beaker cell with three-electrode setup. The reference and counter electrodes were Ag/AgCl and graphite rod, respectively. The electrolyte was 0.5 mol dm^{-3} H_2SO_4. LSV, CA, and CV were measured using multichannel electrochemical measurement systems (Hokuto Denko HZ-Pro and Parstat MC).

Terahertz time domain spectroscopy (THz-TDS). THz-TDS was performed using the self-made instrument, which has used in the other literatures.[75,77,81,82,84] The light source was an ultrafast pulse fiber laser (FemtoFErb780, TOPTICA, 780 nm, 100 fs, 50 MHz). Dipole photoconductive antennae (SD-TX101 and SD-RX101, Pioneer) were used as the source and detector of THz waves. At the sample position, we applied an attenuated total reflection (ATR) setup using a Dove prism made of silicon (refractive index 3.4) for accurate determination of the complex dielectric functions of the aqueous solutions.[S1,78] The THz wave was set to be *p*-polarized at the prism surface. The penetration depth of the evanescent field of the THz wave was approximately 20 μm. The optical length of one of the split infrared lights was changed by using a delay stage (SGSP(GS)26-50, SIGMAKOKI Co. Ltd.). The entire system was purged with dry air (QD-20-50 and RD-45-N, IAC. Co., Ltd.). The lock-in detection technique (SR830 DSP, Stanford Research System) was used. With the use of this setup, the complex dielectric constants were determined with high precision and reliability in the 0.3−2.5 THz region. During the measurements, the temperature of the ATR sample cell was maintained at 25 °C by using a Peltier device (TDC-1010A, Cell System Co., Ltd.). The measurements were performed at least 4 times for one sample, and the results were averaged.

Analysis of hydration state. The samples of BQ-Py, BQ-BO, AB, GO, graphite, and GC were dispersed at 10 wt% in 1 mol dm^{-3} NaOH aqueous solution at room temperature. The homogenous dispersion liquids of BQ-Py and BQ-BO were used for THz-TDS. To subtract the effect of hydration of NaOH from the hydration in the whole aqueous solution, we first performed THz TDS of pure water and 1 mol dm^{-3} NaOH solution. By fitting the pure water results (the imaginary part of the dielectric constant) with eqn (2) in the main text, we obtained all parameters, which agreed well with the reported value.[87] For the fitting to the results of NaOH solution, we fixed parameters other than $\Delta\varepsilon_{\mathrm{slow}}$, $\Delta\varepsilon_{\mathrm{fast}}$ and A_s to those of pure water. The hydration effect of NaOH was evaluated by substituting $\Delta\varepsilon_{\mathrm{slow}}$, $\Delta\varepsilon_{\mathrm{fast}}$ obtained here into eqn (3) in the main text. Since NaOH was found to exhibit negative hydration,[88] the amount of hydration was calculated to be negative. Based on the density of the 1 mol dm^{-3} NaOH solution (1.04 g/cm^3), c =1.00301 was determined. Next, we measured solutions of BQ-BO or BQ-Py dissolved in NaOH. Again, we fixed parameters other than $\Delta\varepsilon_{\mathrm{slow}}$, $\Delta\varepsilon_{\mathrm{fast}}$ and A_s to those of pure water. Using obtained $\Delta\varepsilon_{\mathrm{slow}}$, $\Delta\varepsilon_{\mathrm{fast}}$, we calculated total hydration amount by eqn (2) in the main text for the BQ-BO (or BQ-Py) and NaOH. The hydration amount of BQ-BO or BQ-

Py itself was obtained by subtracting the hydration amount obtained from the NaOH-only solution from the total amount. As NaOH showed negative hydration, the hydration of BQ-BO (or BQ-Py) itself was more than the total hydration amount of the solution.

Additional References

S1. M. Nagai, H. Yada, T. Arikawa and K. Tanaka, *Int. J. Infrared Millim. Waves*, 2006, **27**, 505.

Summary of the catalytic performance in previous works

Table S1. Overpotential, Tafel slope, and synthetic temperature of metal-free HER catalysts in previous works.[36–58]

No.	Materials	ΔE @10 mA cm^{-2} / mV	Tafel slope / mV dec^{-1}	Category	Synthetic temperature / °C	Ref.
1	N-doped graphene	474	172	Heteroatom-doped graphene	500	36
1	S-doped graphene	391	130	Heteroatom-doped graphene	500	
1	N, S-doped nanoporous graphene	276	81	Heteroatom-doped graphene	500	
1	N-doped graphene	559	232	Heteroatom-doped graphene	800	
1	S-doped graphene	480	230	Heteroatom-doped graphene	800	
1	N, S-doped nanoporous graphene	385	105	Heteroatom-doped graphene	800	
2	N-doped graphene (HT-AFNG)	350	113	Heteroatom-doped graphene	180	37
2	N-doped graphene (AFNG)	372	120	Heteroatom-doped graphene	180	
3	nanoporous-graphene	650	139	Carbon	750	38
3	N-doped nanoporous-graphene	550	163	Heteroatom-doped graphene	900	
3	S-doped nanoporous-graphene	440	118	Heteroatom-doped graphene	900	
3	P-doped nanoporous-graphene	430	204	Heteroatom-doped graphene	900	
3	SP-doped nanoporous-graphene	380	96	Heteroatom-doped graphene	900	
3	NS-doped nanoporous-graphene	330	105	Heteroatom-doped graphene	900	
3	NP-doped nanoporous-graphene	290	102	Heteroatom-doped graphene	900	
3	NSP-doped nanoporous-graphene	240	90	Heteroatom-doped graphene	900	
4	3D graphene	515	225	Carbon	900	39
4	3D graphene treated by Ar plasma	480	116	Carbon	900	
4	3D S-doped graphene	259	97	Heteroatom-doped graphene	900	
4	3D S-doped graphene treated by Ar plasma	218	64	Heteroatom-doped graphene	900	
5	C3N4 on N-doped graphene	240	51.5	Carbon nitride (C3N4)	600	40
5	C3N4/N-doped graphene mixture	380	67	Carbon nitride (C3N4)	600	
6	graphitic-C3N4 nanoribbons on 2D graphene nanosheets	207	54	Carbon nitride (C3N4)	180	41
7	N-rich honeycomb-like carbon nanosheet derived from silk cocoon	184	191.2	Heteroatom-doped carbon	400	42
7	N-rich honeycomb-like carbon nanosheet derived from silk cocoon	165	179.4	Heteroatom-doped carbon	600	
7	N-rich honeycomb-like carbon nanosheet derived from silk cocoon	165	184.7	Heteroatom-doped carbon	700	
7	N-rich honeycomb-like carbon nanosheet derived from silk cocoon	146	151.9	Heteroatom-doped carbon	800	
7	N-rich honeycomb-like carbon nanosheet derived from silk cocoon	137	131.6	Heteroatom-doped carbon	900	
8	porous C3N4 on graphene	280	143.3	Carbon nitride (C3N4)	550	43
8	porous C3N4 on N-graphene	170	88.6	Carbon nitride (C3N4)	550	
9	N, P-doped carbon (SA900)	419	88	Heteroatom-doped carbon	900	44
9	N, P-doped carbon (SA900Z)	387	80	Heteroatom-doped carbon	900	
9	N, P-doped carbon (SA900C)	204	58	Heteroatom-doped carbon	900	
10	N, S co-doped graphene	340	110	Heteroatom-doped graphene	700	45

10	N, S co-doped graphene	230	72	Heteroatom-doped graphene	500	
10	nanoporous graphene	720	240	Heteroatom-doped graphene	700	
10	nanoporous graphene	670	160	Heteroatom-doped graphene	500	
11	N-doped graphene on glass fiber	336	86	Heteroatom-doped graphene	750	46
12	few layer black phosphors (P) nanosheets	618.3	249	Other materials containing Si and P	25	47
12	few layer P nanosheets on rGO	517.5	210	Other materials containing Si and P	900	
12	few layer P on B-doped graphene	385.9	110	Other materials containing Si and P	900	
13	rGO/O-SiBCN composite	590	127	Other materials containing Si and P	1000	48
14	P, N co-doped porous carbon	241	173.5	Heteroatom-doped carbon	700	49
14	P, N co-doped porous carbon	217	157.4	Heteroatom-doped carbon	800	
14	P, N co-doped porous carbon	150	95.6	Heteroatom-doped carbon	900	
14	P, N co-doped porous carbon	203	136.6	Heteroatom-doped carbon	1000	
15	N, P-codoped carbon nanofiber networks	151	69	Heteroatom-doped carbon	900	50
15	N, P-codoped carbon nanofiber networks	297	167	Heteroatom-doped carbon	900	
16	nitrogenated microporous graphitic frameworks	450	97	COF	350	51
17	p-MWCNTwith acidic oxidation	220	71.3	Carbon	120	52
18	3D N-doped, plasmaetched graphene	128	66	Heteroatom-doped graphene	800	53
18	3D N-doped graphene	262	121	Heteroatom-doped graphene	800	
19	N,S-doped CNFs carbon nanofibers coated with N,P-doped carbon	331	99	Heteroatom-doped carbon	900	54
20	Tp-Bpy-COF	280	100	COF	120	55
21	2D conjugated COFs (2DCCOF1)	541	130	COF	2	56
22	Ultra-thin GDY nanosheets on a 3D carbon fiber network	245	41.6	Carbon	50	57
23	C6-TRZ-TFP COF	200	82	COF	150	58

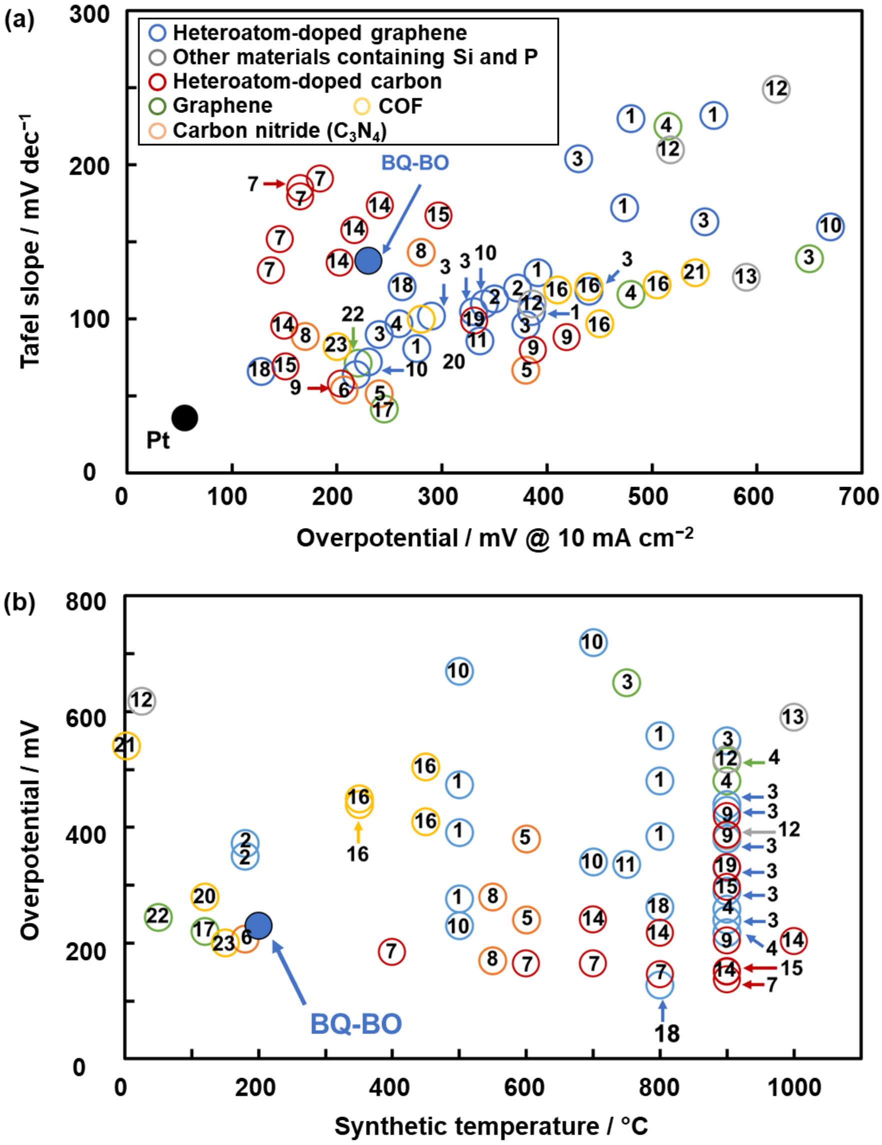

Fig. S1. Summary of HER catalytic performance in previous works. (a) Relationship between ΔE and Tafel slope. (b) Relationship between the synthetic temperature and ΔE. The numbers correspond to those in Table S1.

The heteroatom-doped nanocarbons showed ΔE lower than 150 mV (No. 7, 14, 18 in Table S1 and Fig. S1).[42,49,53] However, the synthetic temperature of the nanocarbons is over 400 °C (Fig. S1b). Although ΔE = 207 and 220 mV were achieved using the graphitic caron nitride on graphene synthesized at 180 °C and the oxidized multi-walled carbon nanotubes treated at 120 °C, respectively (No. 9, 17),[41,52] these catalysts used the nanocarbons synthesized at high temperature. A recent report showed ΔE = 200 mV for the triazine-based COF synthesized at 150 °C for 72 h (No. 23).[58] However, the long-time synthetic process is required.

Training data

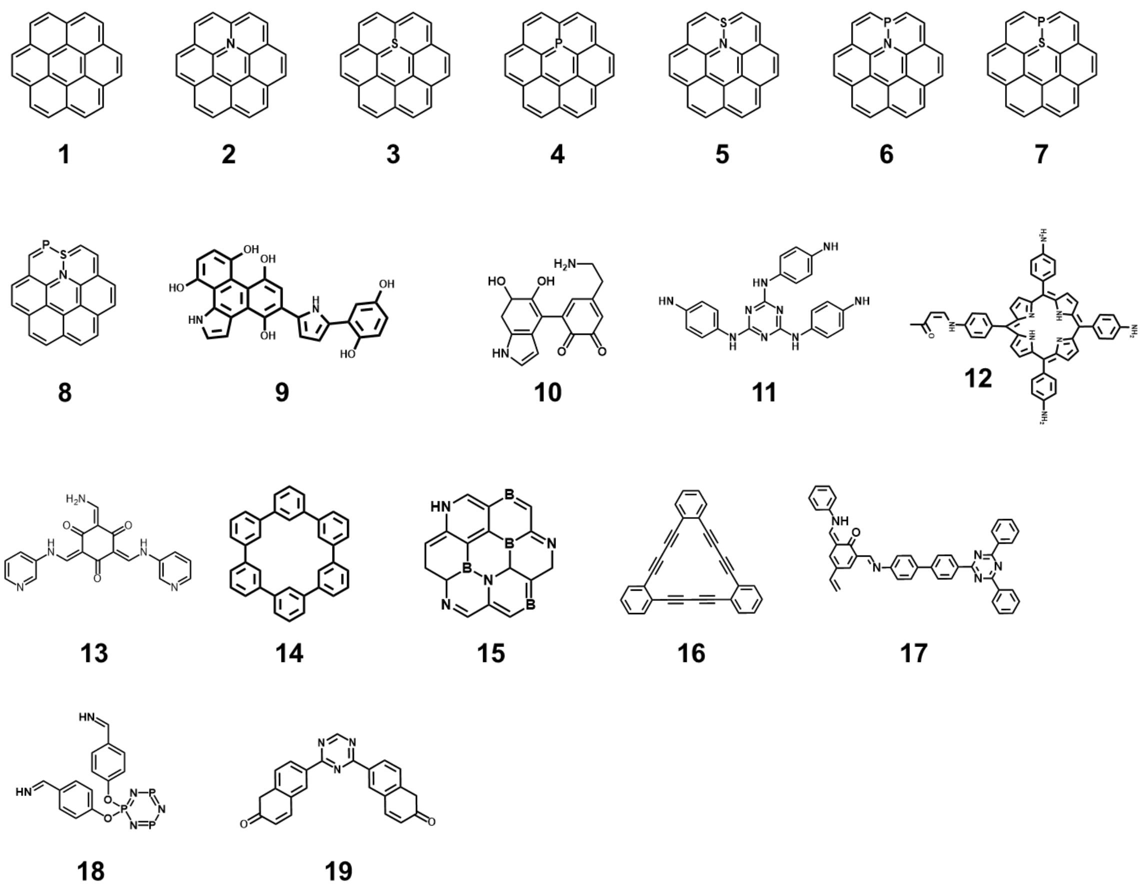

Scheme S1. Molecular structures of compounds **1–19** in the training dataset.

The overpotential of these compounds was referred to the previous reports as follows: **1–8**,[38] **9**,[11] **10**,[59] **11**,[60] **12**,[61] **13**,[55] **14**,[56] **15**,[62] **16**,[57] **17**,[58] **18**,[49] **19**.[63] The repeating units as the minimum partial molecular structure were extracted from the macromolecules, such as graphitic carbons, COFs, and polymers.

Table S2. Training dataset including x_n (n = 1–11) and y of **1**–**19**.

Compounds	x_1	x_2	x_3	x_4	x_5	x_6	x_7	x_8	x_9	x_{10}	x_{11}	y
1	-5.459	-1.428	4.031	4	3.47	267.3	0	42.07	0.101	-0.144	0	-650
2	-3.086	-1.504	1.582	4	4.35	271.46	0.087	42.36	0.338	-0.839	0.0417	-550
3	-4.226	-1.56	2.666	4	4.36	283.42	0.879	30.96	0.647	-0.384	0.0417	-430
4	-4.289	-2.504	1.785	5	17.68	281.01	1.368	35.11	0.448	-0.261	0.0417	-440
5	-4.762	-3.19	1.572	5	6.28	284.73	2.335	36.76	0.195	-0.609	0.0833	-330
6	-4.489	-1.403	3.086	4	4.14	271.96	1.038	38.88	0.6	-0.862	0.0833	-290
7	-4.527	-2.551	1.976	5	6.74	292.63	3.886	30.67	0.227	-0.288	0.0833	-380
8	-4.952	-3.477	1.457	6	7.25	309.64	4.339	35.22	0.203	-0.612	0.125	-240
9	-4.583	-1.024	3.56	3	1.87	382.77	2.911	41.38	0.345	-0.652	0.058824	-277
10	-4.916	-3.25	1.666	2	3.71	213.74	4.619	30.24897	0.347	-0.606	0.1111	-190
11	-5.264	-2.962	2.302	7	8.35	374.53	2.107	33.64595	0.723	-0.675	0.3	-463
12	-4.564	-1.98	2.584	5	5.59	821.29	4.489	39.66	0.423	-0.688	0.140351	-250
13	-5.748	-1.94	3.807	5	6.07	313.46	7.386	32.70994	0.396	-0.655	0.2963	-570
14	-5.873	-1.078	4.795	6	4.83	400.82	0	45.93	0.09	-0.154	0	-541
15	-4.688	-2.134	2.554	5	6.19	263.32	7.153	36.83056	0.38	-0.623	0.333333	-216
16	-5.602	-2.085	3.517	9	7.78	448.65	0.000421	38.06114	0.765	-0.831	0	-68
17	-5.233	-2.432	2.802	8	8.69	666.7	7.061	44.76159	0.456	-0.619	0.102041	-200
18	-5.935	2.629	8.563	8	10.44	447.18	4.589	41.60457	1.143	-0.592	0.333333	-150
19	-6.609	-2.369	4.239	7	9.2	299.27	2.509	42.13051	0.454	-0.532	0.107143	-311

The compounds **1**–**19** were listed in Scheme S1. Table 1 shows the list of the explanatory variables (x_n).

Ten-fold cross validation

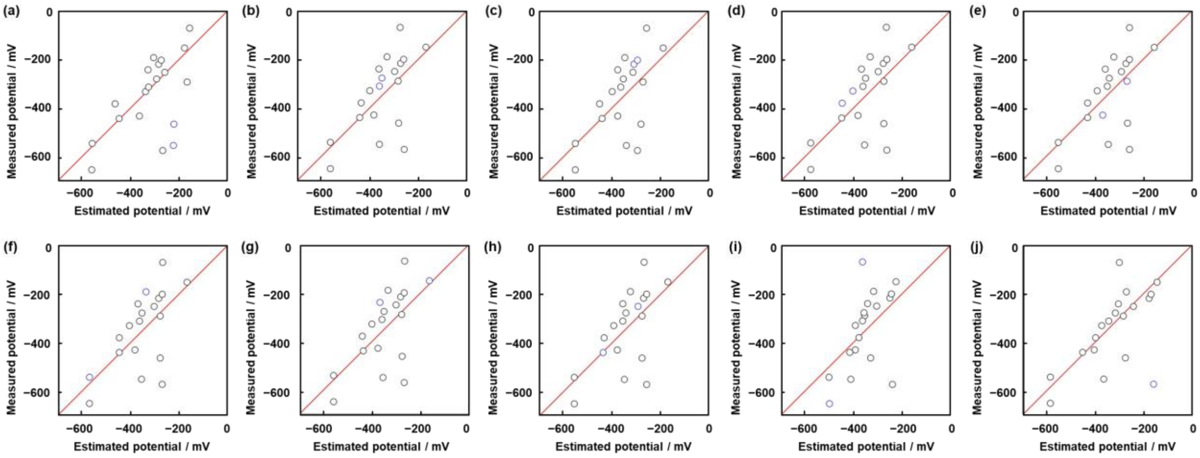

Fig. S2. Relationship between the estimated and measured (reported) ΔE in the ten-fold cross validation of the training dataset.

The dataset was divided into ten segments. After the regression model was constructed using nine segments (17 data) as the training data (black plots in Fig. S2), the validation was performed using one remaining segment (two data) as the test data (blue plots in Fig. S2). The RMSE values were calculated for the training and test. The training and validation were carried out with changing the assignment of the test data to the different segments total ten patterns. The average RMSE value and its standard deviation were calculated to be 118 ± 12.7 mV for the training and 144 ± 118 mV for the test. The RMSE value was consistent with that of the model eqn (1), 121.0 mV. This test implies the validity of the model eqn (1).

Test data for the validation

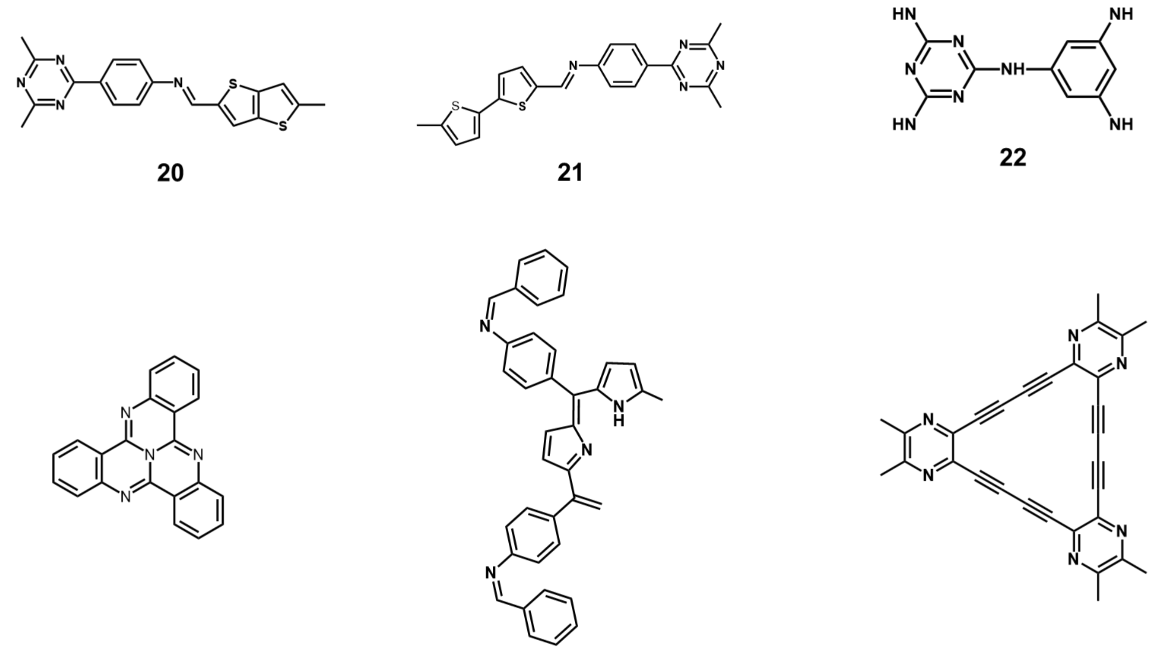
20 **21** **22** **23** **24** **25**

Scheme S2. Molecular structures of compounds **20**–**25** in the test dataset.[64–68]

The overpotential of these compounds was referred to the previous reports as follows: **20**,[64] **21**,[64] **22**,[65] **23**,[66] **24**[67] and **25**.[68] The minimum partial molecular structures were extracted from the macromolecules, such as graphitic carbons, COFs, and polymers.

Table S3. Test dataset including x_n (n = 1–11) and y of **20**–**25**.

Compounds	x_7	x_9	x_{10}	y	y'
20	3.5945	0.427	-0.494	-189	-351
21	3.676549	0.427	-0.496	-151	-349
22	6.376871	0.708	-0.696	-424	-201
23	0.000171	0.54	-0.723	-80	-338
24	4.043497	0.392	-0.790	-185	-281
25	0.000890	0.790	-1.544	-375	-97

The predicted ΔE was calculated based on x_7, x_9, and x_{10} in Table S3 using eqn (1).

XPS profiles of BQ-BO

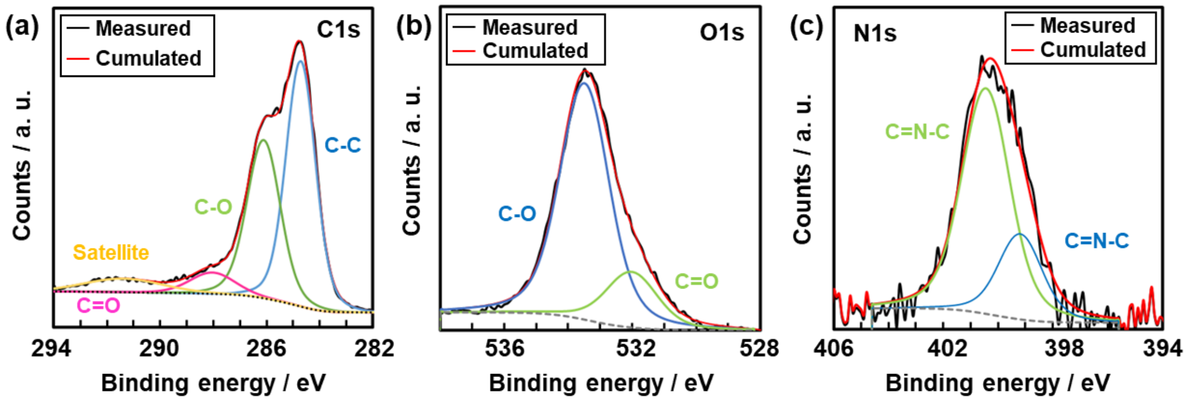

Fig. S3. XPS profiles of BQ-BO. (a) C1s. (b) O1s. (c) N1s.

The profiles indicate that the chemical bonds in the estimated structures in Fig. 1b,c were included in the BQ-BO.

NMR spectrum of BQ-BO

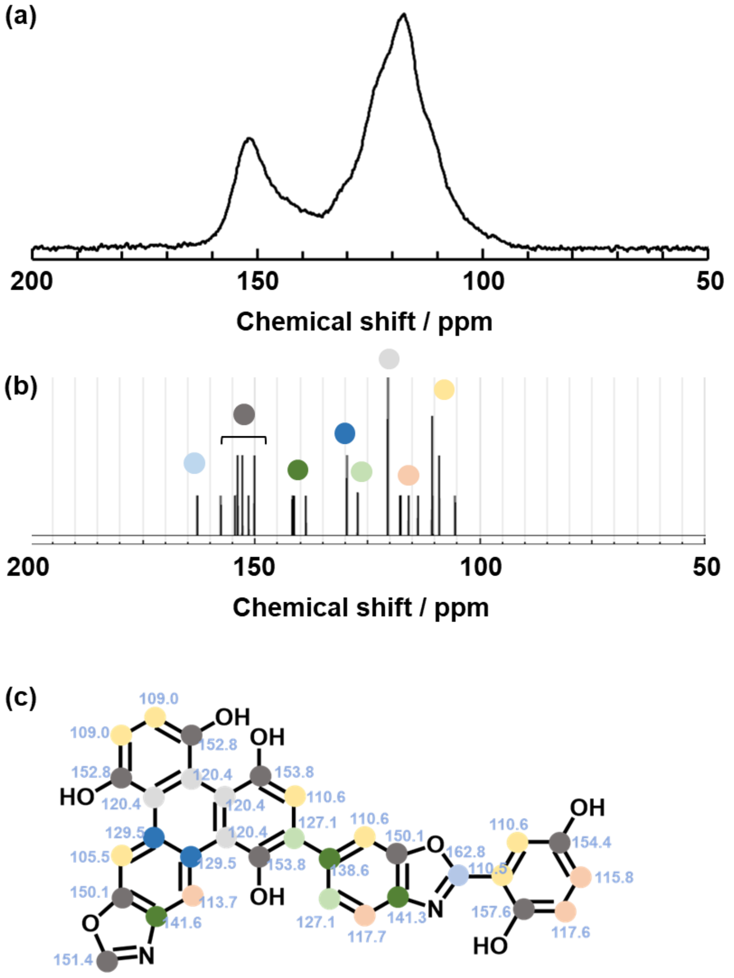

Fig. S4. ^{13}C-MAS-NMR spectra of BQ-BO. (a) Measured spectrum. (b) Calculated spectrum. (c) Calculated chemical shift on each carbon in the structural unit.

The peaks are broadened in the NMR spectrum because of the polymer (Fig. S4a). The calculational simulation was carried out on the representative structural unit of BQ-BO using a free software in http://nmrdb.org/ (Fig. S4b,c). The trace of the peak tops in the calculational spectrum is similar to the curve of the measured spectrum. If the peak broadening originating from the polymerized structure is assumed, the measured spectrum is consistent with the cumulated calculational spectrum based on the estimated structure.

UV-Vis-NIR spectrum of BQ-BO

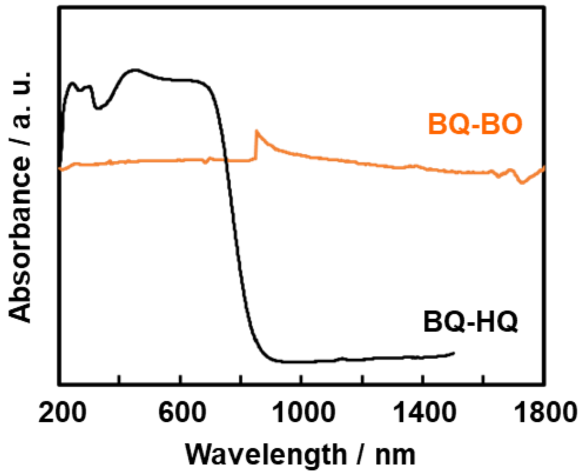

Fig. S5. UV-Vis-NIR spectra of BQ-BO and BQ-HQ.

The BQ-BO network had the absorption in the entire range of visible and NIR regions (Fig. S5). In contrast, the charge-transfer complex of BQ and HQ (BQ-HQ) showed the absorption in the range lower than 800 nm. The results indicate that BQ-BO has the longer extended π-conjugated backbone compared with BQ-HQ. The sawtooth noise around 900 nm was caused by changes of the light source in the spectrophotometer.

SEM and EDX analyses of the bulk BQ-BO particles

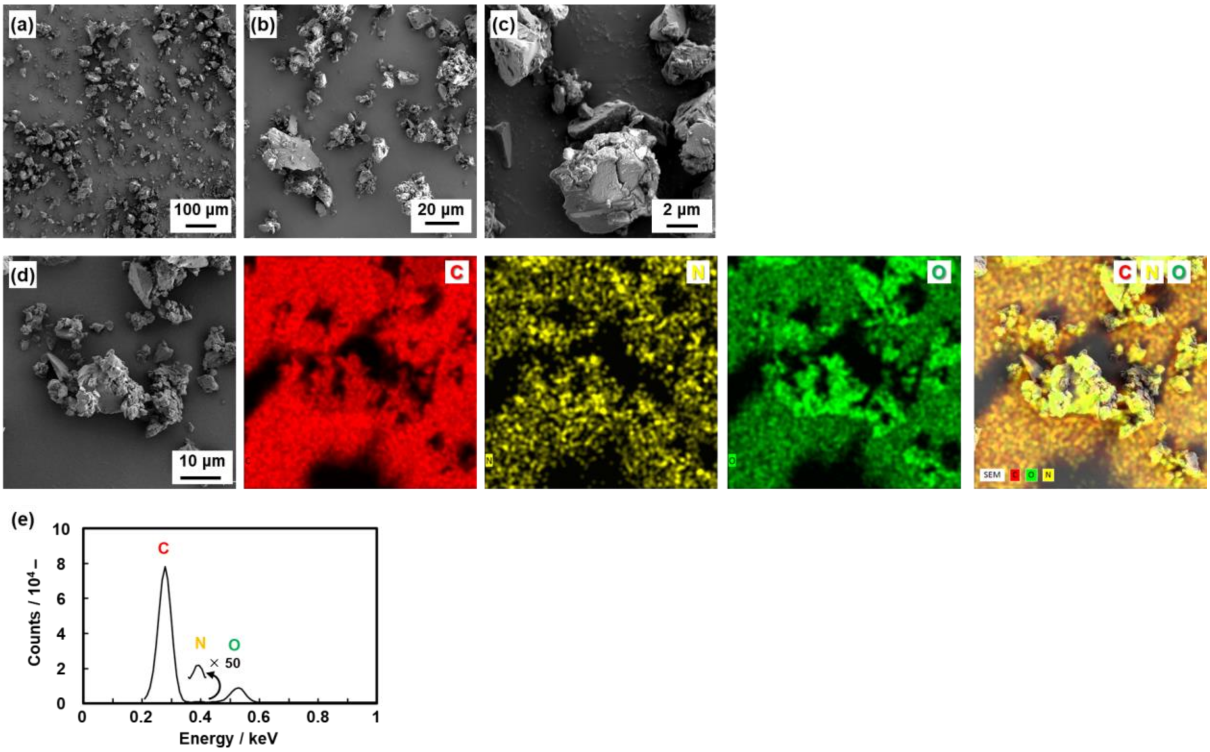

Fig. S6. SEM observations and EDX analyses of the bulk BQ-BO particles before the dispersion in acetone. (a–c) SEM images. (d) SEM image (left), its EDX mappings of each element (middles), and their cumulated image (right). (e) EDX spectrum of the area displayed in the panel (d).

In addition to Fig. 5a in the main text, the SEM images showed the formation of the irregularly shaped particles 1–50 μm in size (Fig. S6a,b). The nanoparticles were not clearly observed in the bulky particles on the magnified image (Fig. S6c). The EDX mapping and spectrum indicate that C, N, and O in the BQ-BO polymer were homogeneously contained in the particles (Fig. S6d,e).

SEM and EDX analyses of the bulk-nano BQ-BO particles

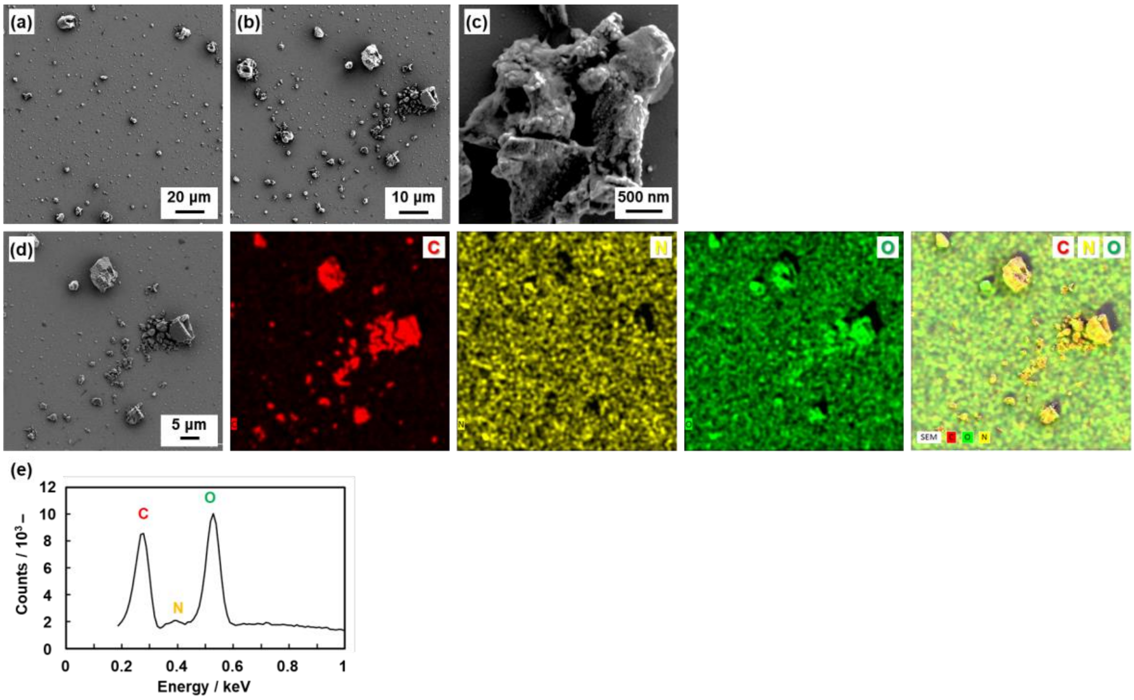

Fig. S7. SEM observations and EDX analyses of the bulk-nano BQ-BO particles before the dispersion in acetone. (a–c) SEM images. (d) SEM image (left), its EDX mappings of each element (middles), and their cumulated image (right). (e) EDX spectrum of the area displayed in the panel (d).

In addition to Fig. 5b in the main text, the SEM images showed the formation of the smaller particles less than 20 μm and nanoparticles (Fig. S7a–c). The EDX mapping and spectrum indicate that C, N, and O in the BQ-BO polymer were homogeneously contained in the particles (Fig. S7d,e).

TEM, SEM, and EDX analyses of the bulk-nano BQ-BO particles

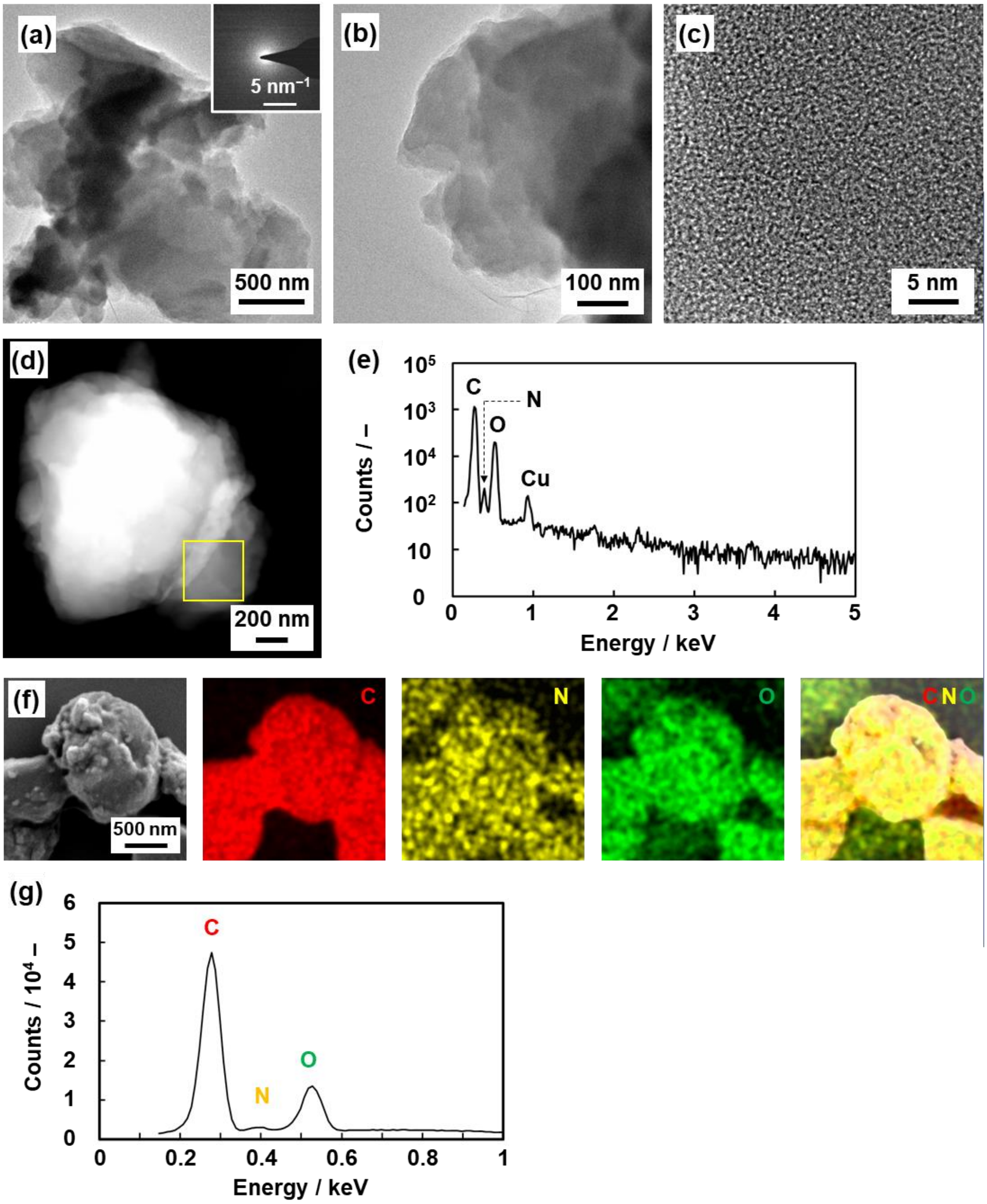

Fig. S8. TEM, SEM, and EDX analyses of the BQ-BO bulk-nano particles after the dispersion in acetone. (a,b) TEM images and SAED pattern (the inset). (c) HRTEM image. (d) High-angle annular dark-field scanning TEM (HAADF-STEM) image. (e) EDX spectrum in the area marked in the panel (d). (f) Magnified SEM image and its EDX mappings of each element (middles), and their cumulated image (right). (g) EDX spectrum of the area displayed in the panel (f).

The additional TEM images support formation of the nanoparticles less than 200 nm, as observed in Fig. 5c,d (Fig. S8a,b). The SAED pattern showed the broadened hallo without the remarkable diffraction spots and rings (the inset of Fig. S8a). The lattice fringes were not observed in the HRTEM image (Fig. S8c). The SAED pattern and HRTEM image support the amorphous nature of BQ-BO. The analyses in the magnified area using HAADF-STEM, SEM, and EDX indicate that the BQ-BO nanoparticle contained C, N, and O (Fig. S8d–g). Note that the peak of Cu in the EDX spectrum is caused by the copper grid.

CV, CA, and LSV curves of BQ-BO

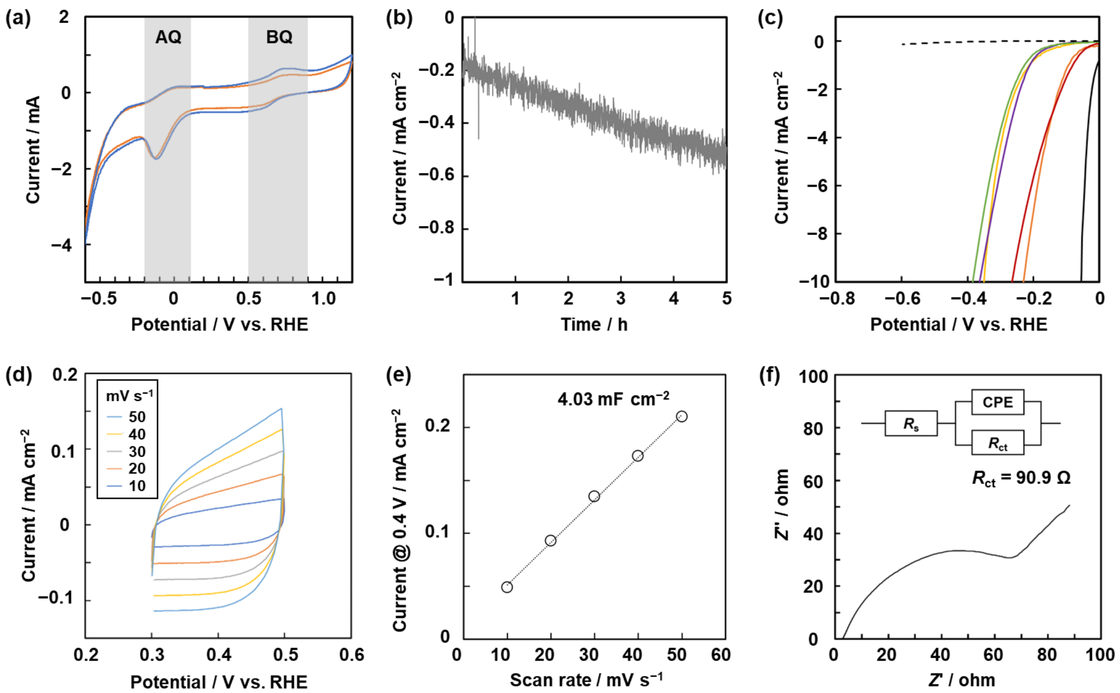

Fig. S9. Electrochemical properties of BQ-BO. (a) CV curves of the two cycles. (b) CA curve at −0.3 V (vs. RHE) for 5 h. (c) LSV curves of the five different BQ-BO samples (colored lines), bare GC electrode (dashed line), and Pt (solid line). (d) CV curves of the BQ-BO bulk-nano sample at the different scan rates. (e) Relationship between the scan rate and sum of the anodic and cathodic currents at 0.4 V (vs. RHE) to estimate the double-layer capacitance from the slope. (f) Nyquist plot of the BQ-BO bulk particles at −0.3 V (vs. RHE).

The two redox peaks around 0 and 0.7 V (vs. RHE) correspond to the redox reactions of AQ and BQ moieties, respectively (Fig. S9a). The CV curve indicates that the reduction is achieved at −0.3 V (vs. RHE). CA at −0.3 V (vs. RHE) was carried out to recover the conjugated structure with reduction (Fig. S9b). The low ΔE was reproducible for the five different BQ-BO samples prepared on GC electrode (Fig. S9c). The average ΔE was 319 ± 68 mV for the five samples. The CV curves were measured in the potential range without the redox reactions (Fig. S9d). C_{dl} was estimated to be 4.03 mF cm^{-2} from the slope (Fig. S9e). The EIS analysis indicates Rct = 90.9 Ω in the equivalent circuit (Fig. S9f).